Liquid Crystalline Nanoconfined Growth of PANI on rGO for Enhanced Electrochemical Glucose Sensing

Anita K. Tawade, [1, $] Praveen Kumar, [2, †, $]Shivaji N. Tayade, [3]Geeta K. Sharma,[4] MeitramNirajLuwang,[5†], Kiran Kumar K. Sharma [1,*]

[1]School of Nanoscience and Biotechnology, Shivaji University, Kolhapur 416004, Maharashtra, India

[2]Science Division, New York University, Saadiyat Island, Abu Dhabi-129188, United Arab Emirates

[3]Department of Chemistry, Shivaji University, Kolhapur 416004, Maharashtra, India

[4]Department of Chemistry Savitribai Phule Pune University, Pune 411007, Maharashtra, India

[5]Chemical Engineering and Process Development (CEPD) Division, CSIR-National Chemical Laboratory (NCL), Pune 411008, Maharashtra, India

***Corresponding author**
Prof. (Dr.) Kiran Kumar K. Sharma
Phone: +91-9881920369
Email: *kks.snst@unishivaji.ac.in*

Synthesis methods for pristine and its intermediate compounds:

Synthesis of graphene oxide (GO) nanosheet: Graphene oxide (GO) was synthesized by Improved Hummer's method[1].

Procedures: Graphene oxide (GO) was synthesized via an improved Hummers' method. Briefly, 3 g of graphite flakes was added to a mixture of concentrated sulfuric acid and phosphoric acid (9:1 v/v). Potassium permanganate (6 wt. equiv.) was slowly introduced into the acid mixture under continuous stirring. The reaction was maintained at 50 °C for 12 h at

150 rpm. After cooling to room temperature, the reaction mixture was poured into 400 mL of ice-cold double-distilled water containing 3 mL of 30% hydrogen peroxide. The resulting suspension was filtered through polyester fibres, and the filtrate was centrifuged at 10,000 rpm for 10 min to collect the solid product. The precipitate was washed successively with 200 mL of distilled water, 200 mL of 30% HCl, and 200 mL of ethanol (twice), followed by a final wash with 200 mL of diethyl ether. The resulting product was dried overnight at 60 °C to yield brown-colored graphene oxide powder.

Synthesis of polyaniline

Polyaniline (PANI) was synthesized following a modified version of the previously reported method for the formation of PANI in a hexagonal crystalline mesophase [2]. In contrast to the original protocol, our approach enabled the formation of PANI in a lamellar mesophase through the incorporation of a co-surfactant, 1-pentanol.

Procedures: As reported in the literature [2], the solution was prepared in a 30 mL sample tube by adding 2 mL of an aqueous solution containing 50 µL of concentrated hydrochloric acid (HCl) and 5 µL of aniline. Subsequently, 1 mL of water and 1 g of cetylpyridinium chloride (CpCl) were added, followed by the addition of the remaining 1 mL of water. A phase separation occurs with organic portion on the top, which contained the monomers. These bottles were kept for solubilisation of the CpCl. After the solution is prepared, 2.99 ml of cyclohexane was added in the mixture and vortex vigorously until the mixture turns into solid white. 1-pentanol was added in small amount in step by step with continuous vigorous vortex until the solid white becomes transparent viscous mixture and starts to slide slowly on the side of the tubes which confirm the transition of hexagonal to lamellar mesophase. 0.0124 gm APS initiator was added and vortexed. The color of the lamellar mesophase changes from colorless to green. The mixture was allowed to polymerize for 24 hrs. The product was then harvested by destabilizing the lamellar mesophase by using isopropyl alcohol (IPA) at 4000

rpm for 10 minutes four times. Finally, polyaniline was harvested and dried at 60˚C for 24 hrs.

Reaction approaches and design of modified SLCLM: Understanding the reactive sites of graphene oxide (GO) is crucial for evaluating its degree of functionalization. GO contains functional groups at both the edges (–C=O, –CHO, –COOH) and basal plane (–OH, epoxide), which serve as potential sites for chemical modification. However, these reactions often proceed through multiple, complex steps due to intrinsic limitations, as illustrated in Scheme 1. Key challenges include restricted molecular orientations of the 2D GO sheets, high activation energies, and surface energy barriers arising from the flat, non-exfoliated nature of GO [3]. While both edge and basal-plane functional groups are theoretically susceptible to selective nucleophilic attack [4], maintaining the 2D morphology of GO during composite synthesis remains challenging. As a result, many functional groups become chemically inaccessible in subsequent transformations.

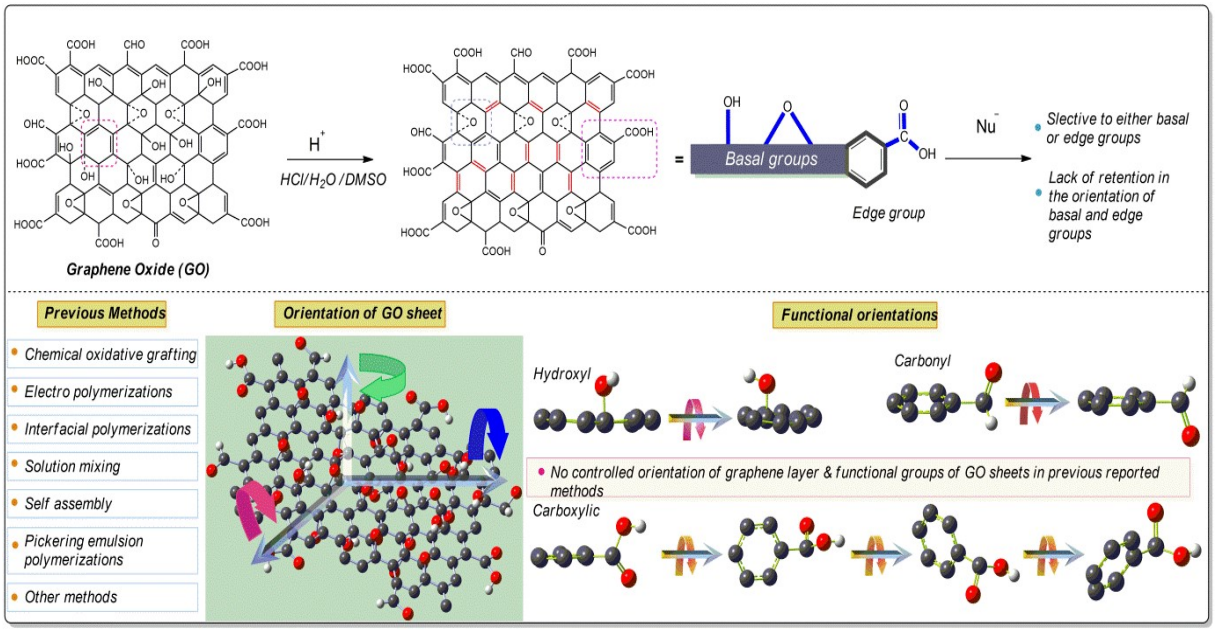

Scheme S1. Contextual study and restrictions in the reaction of GO composite: GO modification via acidification, and restrictions were observed for the GO reactions with aniline/polyaniline in various previously reported methods[5-10];and various types of GO sheet/functional group's orientations along with conformational phase transitions[11-13].

In most GO-based nanocomposites, physical interactions with other nanomaterials predominate due to limited chemical accessibility of functional groups[14, 15]. To address the structural constraints imposed by GO's planar geometry, a critical strategy involves preserving the intrinsic 2D morphology and the spatial orientation of functional groups on both the basal and edge planes during synthesis (as previously illustrated in **Scheme 1**). These conditions are essential for enabling concurrent chemical modifications at multiple reactive sites. The current study overcomes these challenges through the use of a bi-solvent self-limiting confined lamellar mesophase (SLCLM) method, which maintains the planar integrity of GO and promotes simultaneous nucleophilic reactions across its functional landscape, thereby achieving effective chemical transformation.

Synthesis of intermediate edge side product (N-phenyl anthranilic acid derivative):

A novel, cost-effective, and facile synthetic route for the preparation of N-phenyl anthranilic acid derivatives has been successfully developed, offering a more accessible and operationally simple alternative to previously reported methods [16].

Procedures: In a round-bottom flask, 400 µL of aniline was combined with 1 g of benzoic acid and 0.2 g of the surfactant CpCl in 100 mL of double-distilled water (DDW). The reaction mixture was stirred continuously at 500 rpm for 1-2 hours to ensure complete solubilization. The resulting milky-white solution was transferred to a separatory funnel, followed by the addition of 100 mL of benzene for extraction of the synthesized N-phenyl anthranilic acid derivative. The mixture was vigorously shaken, then allowed to settle for 30 minutes. The upper benzene layer, appearing as a light golden-yellow phase, was separated from the lower aqueous layer containing unreacted CpCl (milky white). The product was isolated as crystalline N-phenyl anthranilic acid derivative by rotary evaporation of the benzene fraction (see **Scheme S2**).

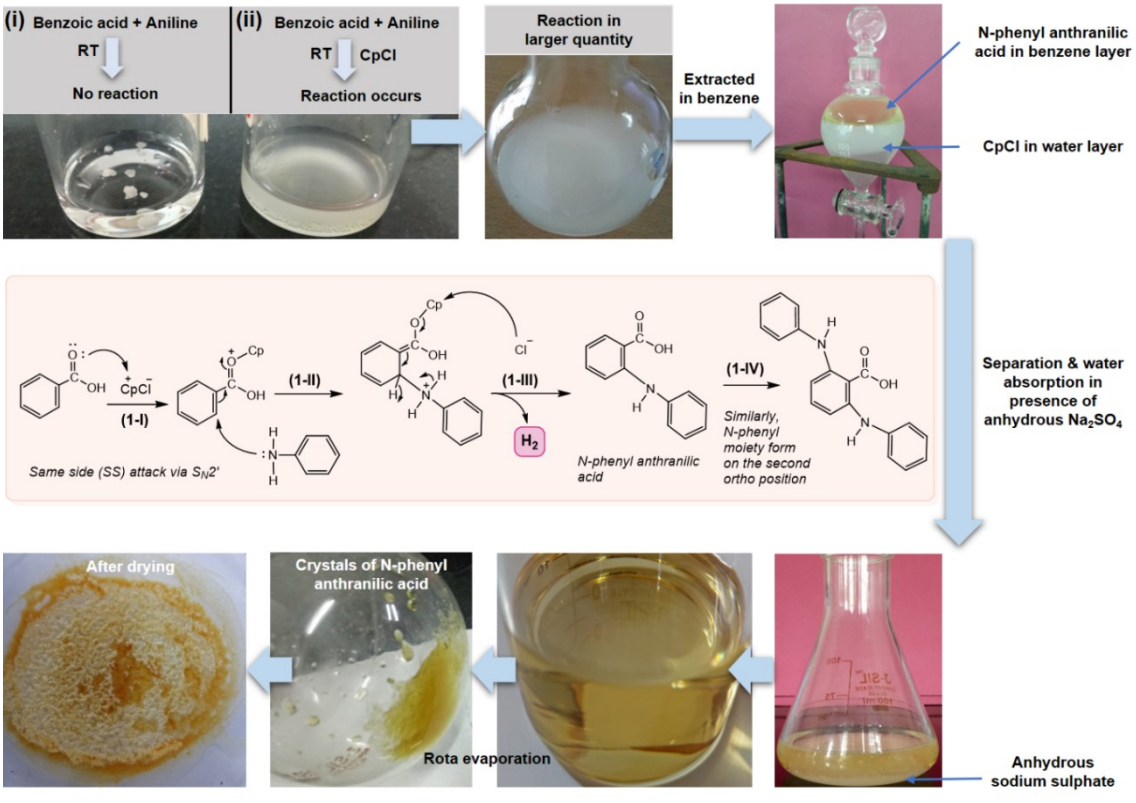

Scheme. S2.A novel one-pot synthesis method was developed for the formation of N-phenyl anthranilic acid derivative crystals via a room-temperature reaction of benzoic acid with aniline in the presence of the surfactant CpCl.

In the absence of CpCl, no reaction between aniline and benzoic acid was observed, as depicted in **Scheme S2(i).** The addition of CpCl initiates the reaction, as shown in **Scheme S2(ii)**. A plausible mechanism is proposed in **Scheme S2**, wherein CpCl acts as an electrophile, generating acidic sites at the ortho (2,6) positions of benzoic acid, facilitating nucleophilic attack by aniline monomers and leading to the formation of the N-phenyl anthranilic acid derivative with concurrent evolution of H_2 gas. Mechanistic confirmation and product characterization were achieved via gas chromatography (GC), ^{1}H and ^{13}C NMR, and high-resolution mass spectrometry (HRMS), as detailed in **Figure S11**.

Procedures used for the detection of H_2 and CO_2 evolution in rGO-PANI:

By taking of 20 µL aniline monomer in a round bottom (RB) flask which was followed by addition of 200 µL (0.107M) conc. HCl, the aniline monomers are converted into aniline hydrochloride. 8 gm of CpCl(cationic surfactant) and 1.8 ml of 0.5 mg/mL graphene oxide in DMSO were added to the aniline hydrochloride solution followed by further addition of 8mL nano-pure water for desolation of surfactant. The RB was kept for solubilization and then poured 12 mL of cyclohexane. Simultaneous vortex the RB by adding 1-pentanol (co-surfactant) drop wise until solution becomes clearly lamellar mesophase (up to 1.5 mL). After lamellar mesophase is formed, add 0.05 g (6.2 ppm) ammonium per sulphate (APS) as an initiator and kept for 24hrs for the polymerization reaction to occur.

Study of rGO-PANI compounds through various characterizations:

Study of FTIR spectra:

The formation of –C–N– bonds occurs at two distinct sites: (i) on the GO surface and (ii) between GO layers. According to the Beer–Lambert law, absorbance (A) is proportional to absorptivity (ε), concentration (c), and path length (l), where ε is related to the square of the change in dipole moment with respect to bond displacement $(d\mu/dx)^2$. During vibrational modes, both peak intensity and position are influenced by changes in dipole moment and bond length. Surface –C–N– bonds exhibit unconstrained vibrations at 1108 cm^{-1} (U) with a large dipole moment change, resulting in a high dμ/dx and an intense absorption peak. In contrast, interlayer –C–N– bonds experience restricted vibrations, leading to a reduced dμ/dx and a less intense peak at 1226 cm^{-1} (L). Additionally, a new hydroxyl group formed via epoxide ring opening displays higher wavenumber absorption at 1480 cm^{-1} compared to both –C–N– and pristine hydroxyl vibrations. This shift arises from resonance and the negative inductive (–I) effect of the '–N–' atom in the PANI moiety bonded to the GO basal plane, which reduces the sp^3 character at carbon-2, thereby strengthening the –C–OH bond (Figure. S1a).

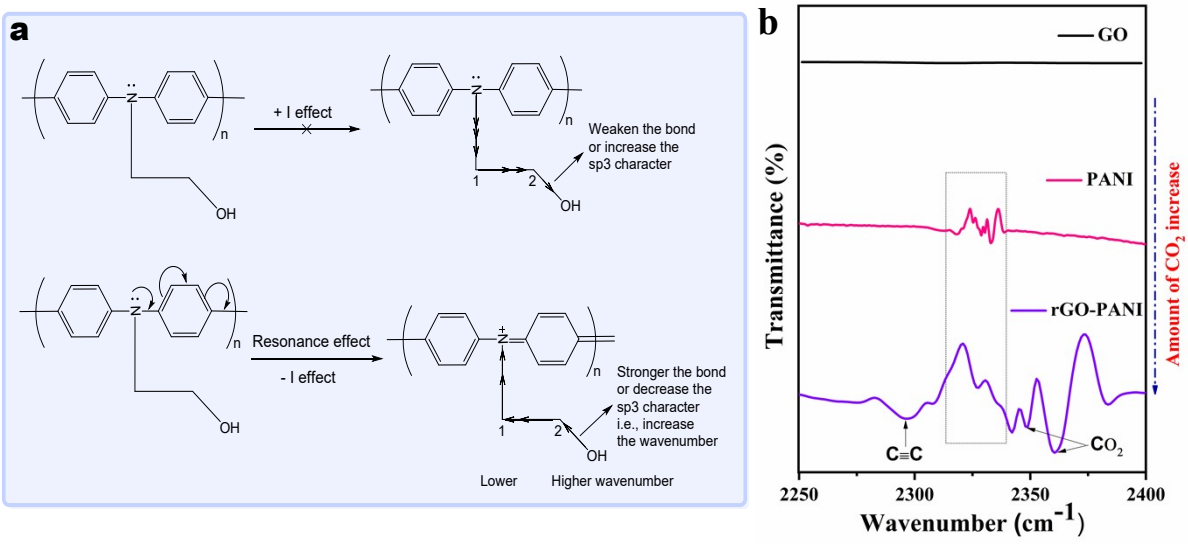

Fig. S1.(a) Schematic illustration of inductive and resonance effect in rGO-PANI,(**b**)FTIR spectra of GO, PANI and rGO-PANIto confirmed the CO_2removal during the synthesis of rGO-PANI.

Study of Raman spectra:

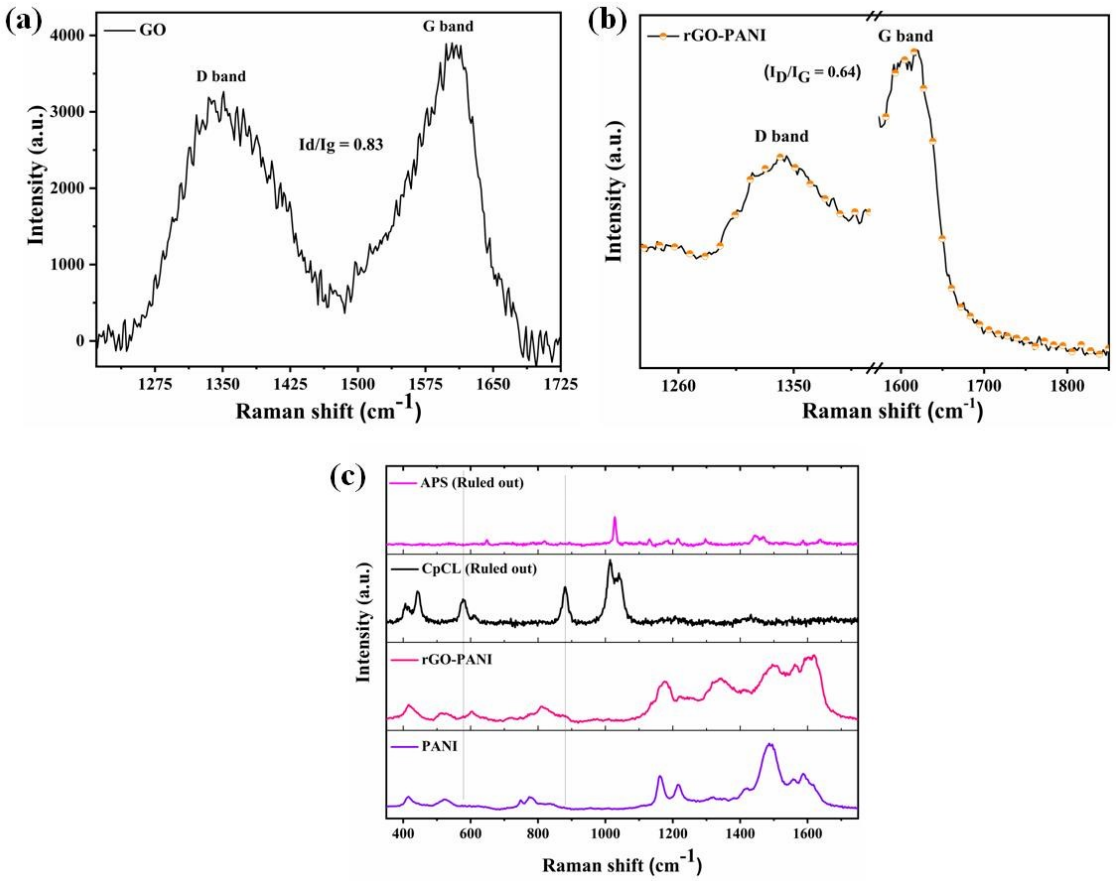

Fig. S2. Analysis of Raman spectra: (a) Raman spectrum of pristine synthesized GO with determination of the ID/IG ratio. (b) Calculation of the ID/IG ratio for rGO-PANI. (c) Comparative Raman spectral analysis of rGO-PANI alongside its precursors, ammonium persulfate (APS), cetylpyridinium chloride (CpCl), and polyaniline (PANI).

3.3. Study of ^{13}C SSNMR spectra of rGO-PANI and pristine compounds:

The rGO-PANI nanocomposite, along with pristine GO and polyaniline, was characterized using ^{13}C solid-state NMR spectroscopy (**Figure S3**). The ^{13}C NMR spectrum of rGO-PANI

(**Figure S3b**) notably lacks peaks corresponding to pristine GO functional groups, such as epoxy (60 ppm), hydroxyl (70 ppm), and carboxyl (168 ppm) groups observed in GO (**Figure S3a, c**) [17], indicating substantial modification of the GO carbon framework, consistent with Raman analysis of the D/G peak ratio and profiles [18]. Instead, new resonances appear between 85 and 125 ppm, attributed to the formation of novel bonds linking the 2D GO sheets and polyaniline chains. Specifically, peaks at 98, 108.3, 114, and 121.6 ppm (**Figure S3b**) correspond to -C–OH, -C≡C–, -C–N– bonds, and additional sp^2 carbons, as confirmed by deconvolution (**Figure. 2c**). Notably, shifts in the chemical shifts of the -C–N– and newly formed –C–OH bonds, relative to pristine polyaniline and GO, respectively, are observed and can be rationalized by nuclear Overhauser effect (NOE) interactions (**Figure S3a-c**). These chemical shift variations are further supported by literature reports on structurally analogous moieties such as 1-amino-2-naphthol (A), 3-amino tetrahydro naphthalen-2-ol (B), and N-phenyl tetrahydro-isoquinoline (C), as illustrated in **Scheme S3** [19–21].

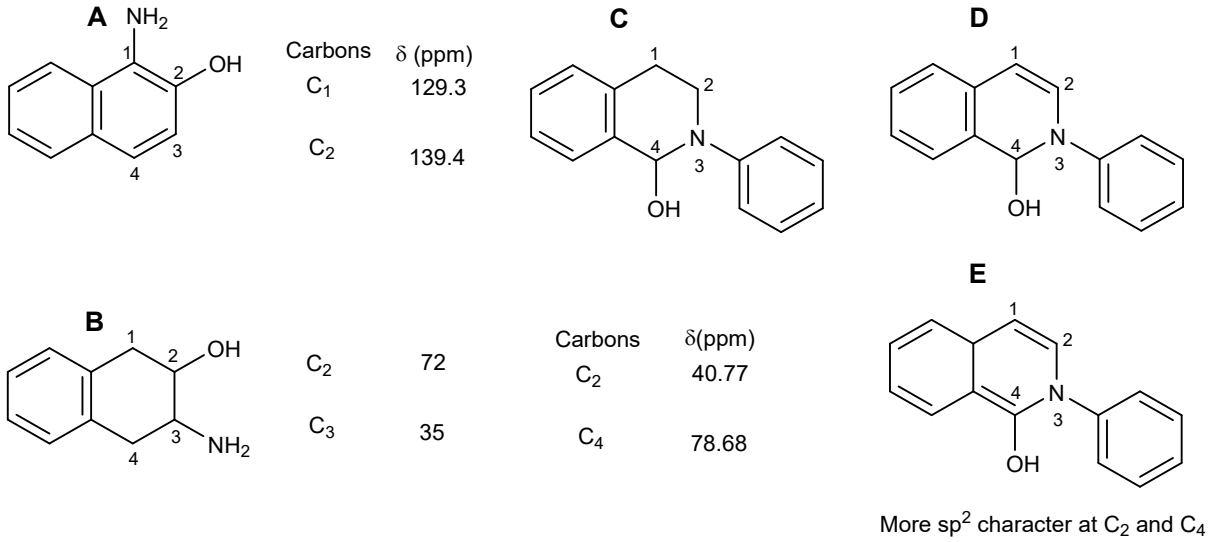

Scheme S3. Comparative analysis of chemical shift (δ = ppm) values of previously reported in ^{13}C NMR of amino and hydroxyl carbons at 1, 2 positions from each other [17-19] and their comparisons with^{13}C NMR δ values of amino and hydroxyl carbons of rGO-PANI.

However, the chemical environment of amino (C_2) and hydroxyl (C_4) carbons (at 2, 4 positions) in rGO-PANI framework are not entirely similar. This can be understood from the structure A, a fully conjugated carbon (C_1 and C_2) compound with δ values 129.3 and 139.4 ppm respectively, while structure B and C possesses comparatively less saturated environment with δ values 70-80 and 35-40 ppm corresponding to -C-OH and -C-N- bonds respectively (**Scheme. S3**). As GO possesses hexagonal arrangement of numerous carbon atoms in a 2D sheet, therefore amino (C_2) and hydroxyl (C_4) carbons should fall in similar category if there is any change in the conjugation (sp^3 to sp^2) in their carbon skeletal as illustrated in structure D and E (**Scheme S3**). Therefore, the δ values of carbon in rGO-PANI are expected to be higher than that of B and C but should be less than D and E carbon skeletal arrangements. Further, due to heterogeneous distribution of sp^3 and sp^2 chemical environment, the δ values of rGO-PANI carbons are expected in between B, C and D, E.

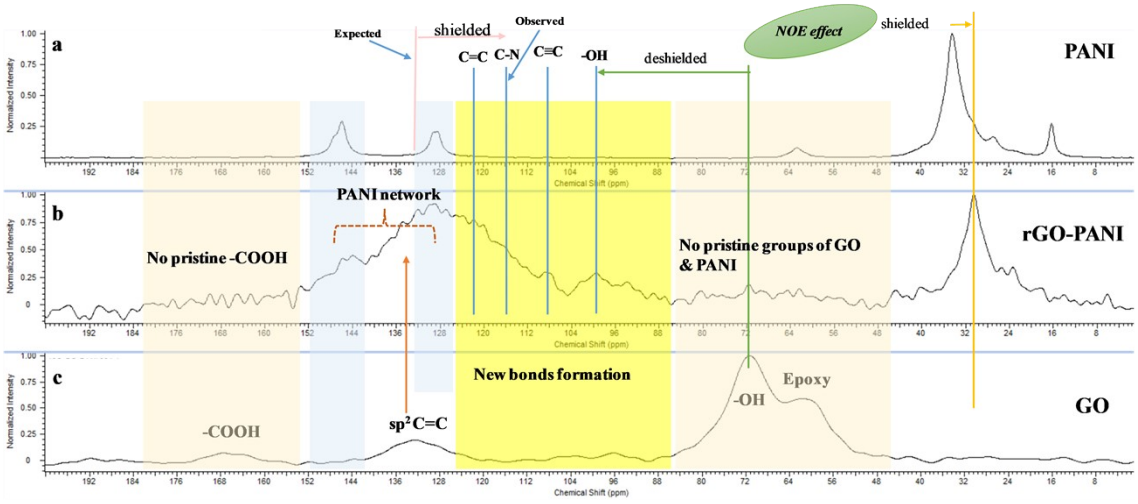

Fig. S3.(a-c).SSNMR spectra:^{13}C Solid-state−nuclear magnetic resonance (SS−NMR) spectra: Solid-state CPMAS NMR were measured with the probe H164388_0001 PH MAS DVT 500W2 BL4 N-P/F/H through pulse sequence cross polarization(cp) using a [400 MHz] JEOL 400 spectrometer operating for a ^{13}C Larmor frequency of 75.47 MHz with a number of transients (43602). Cross-polarization magic angle spinning (CPMAS) was recorded with

0.0451 s recycle time and 16384 scans. SW (cyclical) (Hz) 22727.27, spectrum offset (Hz) 7521.0117, and sweep width (Hz) 22725.89 at a temperature of 21.0 °C. The ^{13}C chemical shift was calibrated against TMS (δ = 0 ppm).

3.4. Analysis of XPS spectra:

X-ray photoelectron spectroscopy (XPS) analysis confirms the formation of covalent –C–N– bonds between polyaniline (PANI) and graphene oxide (GO), as well as the partial reduction of GO to reduced graphene oxide (rGO) through the generation of additional sp^2 and acetylenic (sp) carbon species. To accurately interpret the chemical bonding environments, charge correction in the C 1s, N 1s, and O 1s core-level spectra of all samples was performed using the Si 2p core-level binding energy as a reference (**Figure S4a, b**) [22].

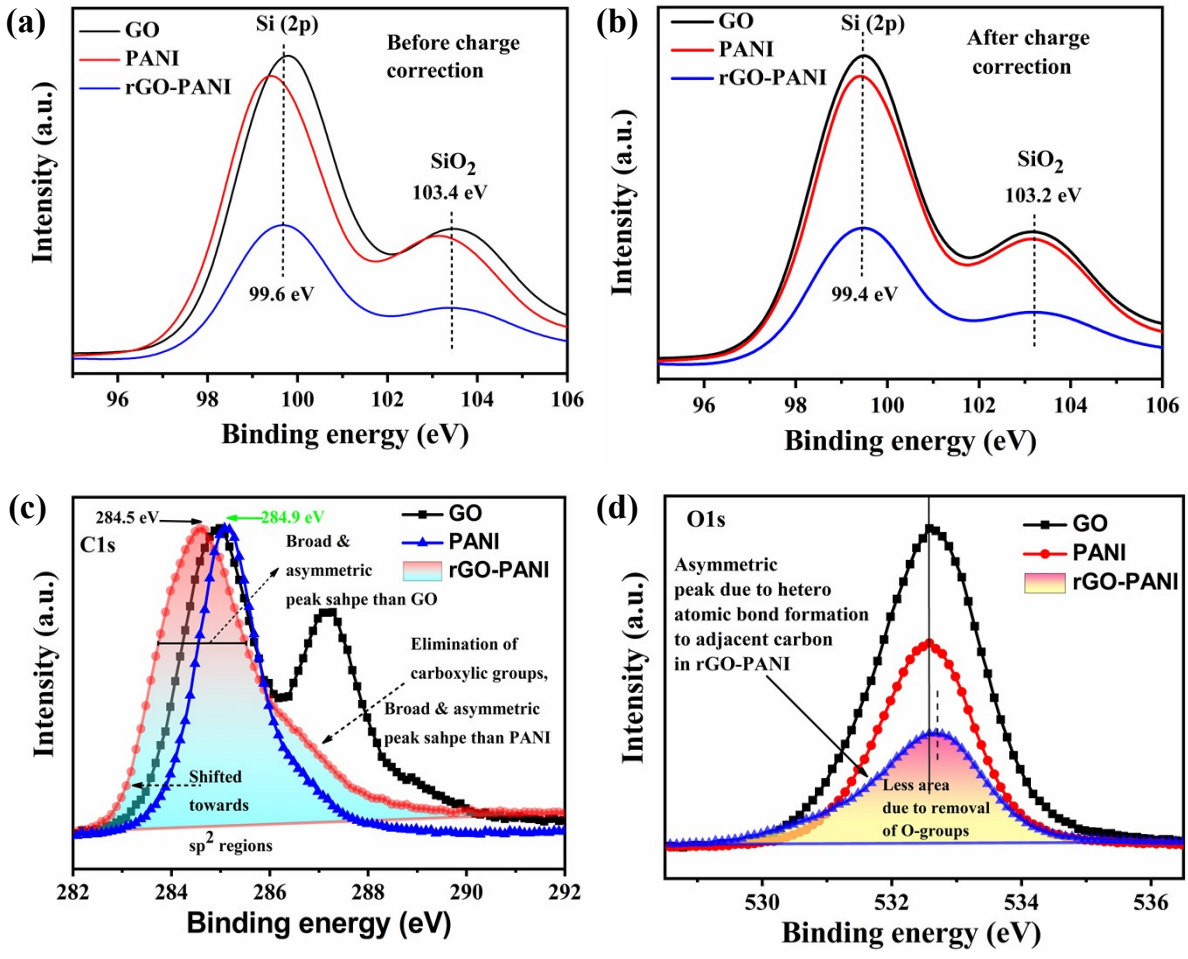

Fig. S4. Analysis of XPS spectra: (a-b) Si2p core-level spectra observed in GO, PANI and rGO-PANI; before and after charge correction,(**c-d**)C1s and O1s spectra of GO, PANI and rGO-PANI respectively.

The deconvoluted C 1s and N 1s spectra (main text Figure. 3c,d) reveal the presence of sp^2 and sp (acetylenic) carbon [23–26], –C–OH groups, and covalent –C–N– linkages, confirming the chemical interaction between GO and PANI [27–28]. Notably, the C 1s core-level peak of rGO–PANI shifts from 284.9 eV to 284.5 eV, indicative of increased sp^2 carbon content. Additionally, the emergence of a broad and asymmetric peak top, compared to pristine GO and PANI, suggests the formation of a hybrid sp/sp^2 carbon network in the rGO–PANI composite (**Figure S4c**).Further, the asymmetric broadening at the lower binding energy side of the C 1s spectrum supports the formation of covalent –C–N– linkages between PANI and GO. The disappearance of the peak at 287.2 eV in rGO–PANI strongly indicates the decarboxylation of GO, likely through CO_2 release.

Similarly, the O 1s spectrum of rGO–PANI exhibits broader and more asymmetric features than those of pristine GO and PANI, reflecting the formation of heteroatomic –C–N– bonds and a hybridized carbon network. A noticeable decrease in the O 1s peak area further corroborates the effective removal of oxygen-containing functional groups in rGO–PANI (**Figure S4d**), consistent with partial reduction of GO and improved structural stability.

3.5. Elemental mapping, EDS and SEAD

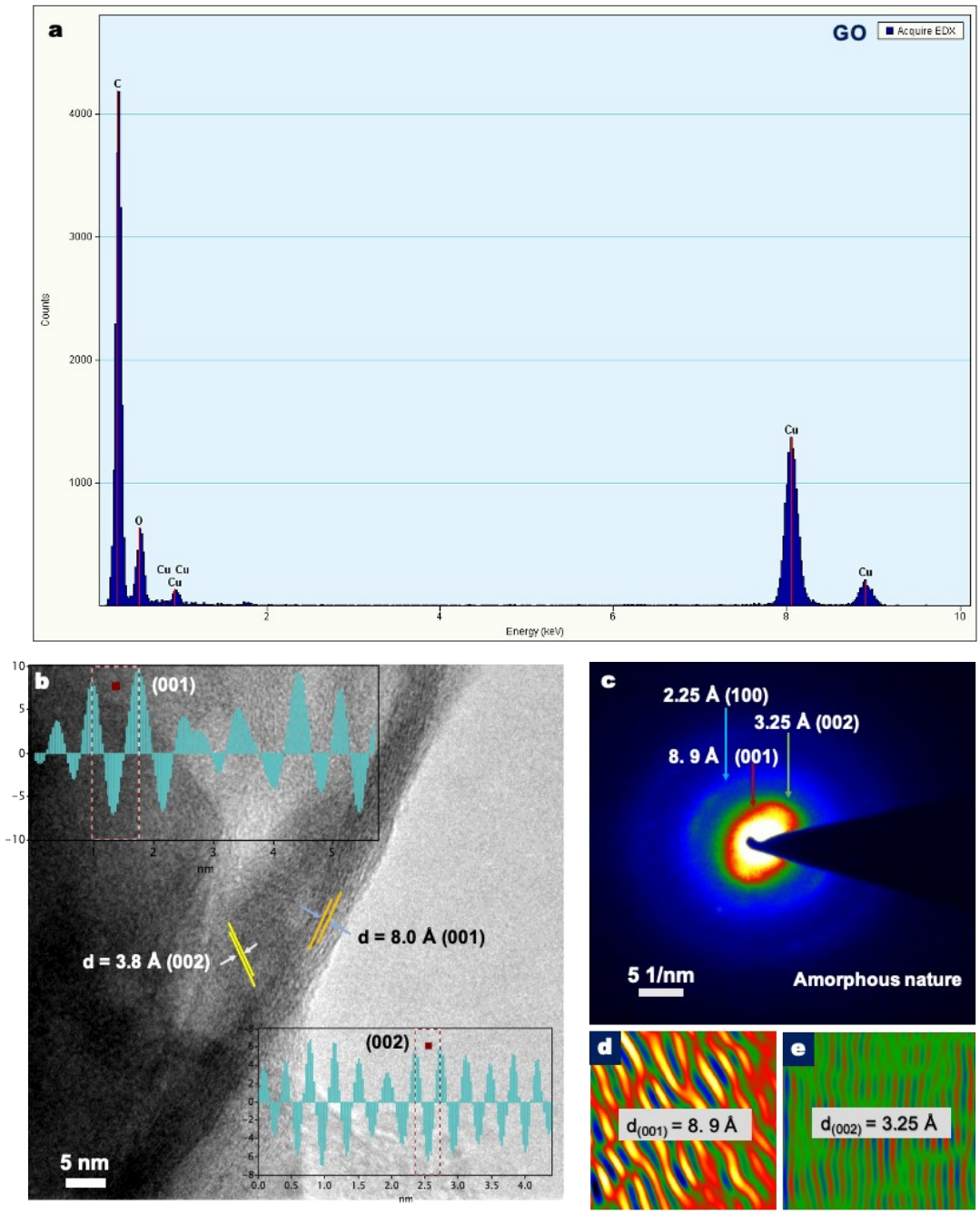

Fig. S5.(a) Energy-dispersive X-ray spectroscopy (EDS) analysis confirms the elemental composition of pristine graphene oxide (GO). (b) High-resolution transmission electron microscopy (HR-TEM) reveals nanoscale features with measured interplanar spacings of 3.8 Å and 8.0 Å, corresponding to the (002) and (001) crystallographic planes of GO, respectively (inset). (c) Selected area electron diffraction (SAED) pattern indicates the amorphous nature of GO, with observable diffraction rings assigned to the (001), (002), and (100) planes, exhibiting d-spacings of 8.9 Å, 3.25 Å, and 2.25 Å, respectively. (d,e)

Simulated fringe patterns corresponding to the (001) and (002) planes further corroborate the structural analysis of GO.

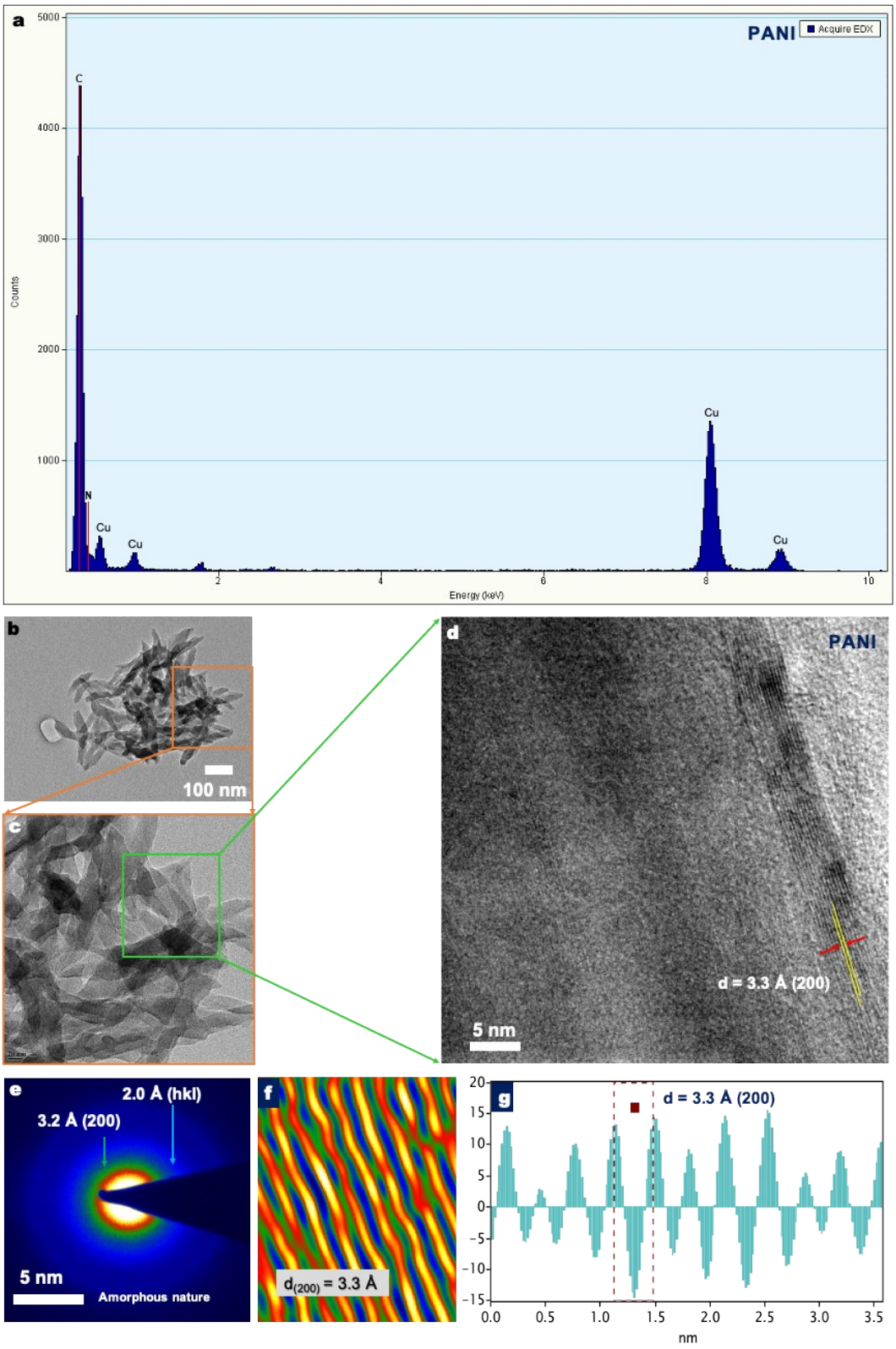

Fig. S6.(a) Energy-dispersive X-ray spectroscopy (EDS) confirms the elemental composition of pristine polyaniline (PANI). (b,c) High-resolution transmission electron microscopy (HR-TEM) images reveal the nanostructured morphology of PANI. (d) HR-TEM fringe analysis displays lattice fringes with an interplanar spacing of 3.3 Å. (e,f) Selected area electron

diffraction (SAED) and corresponding simulated fringe patterns indicate the amorphous nature of PANI, with a discernible (200) plane exhibiting a d-spacing of 3.3 Å.

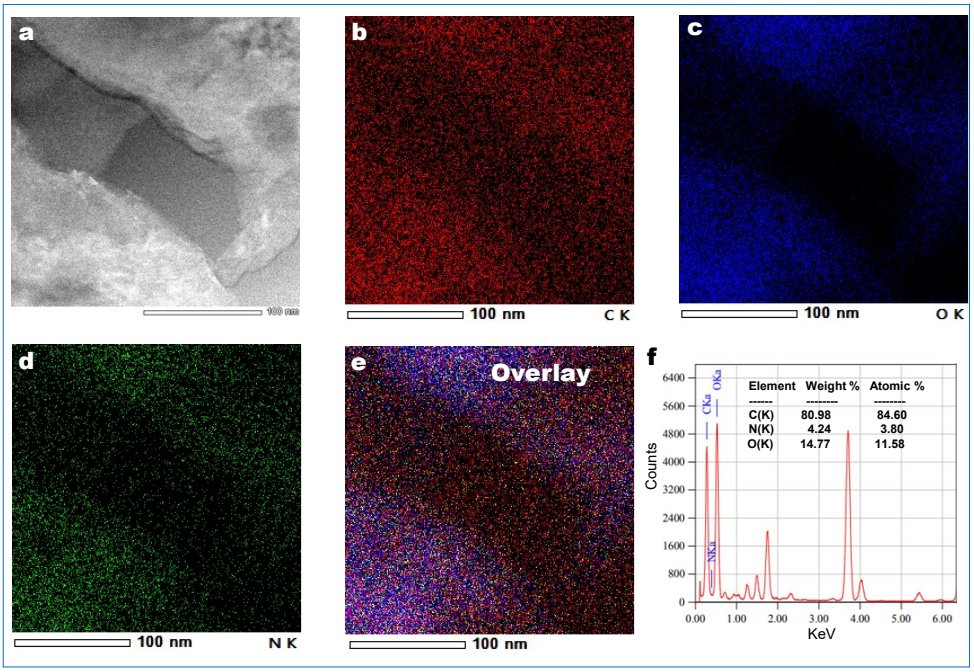

Fig. S7.HAADF-STEM elemental mapping of rGO-PANIat nano-level through HR-TEM analysis.

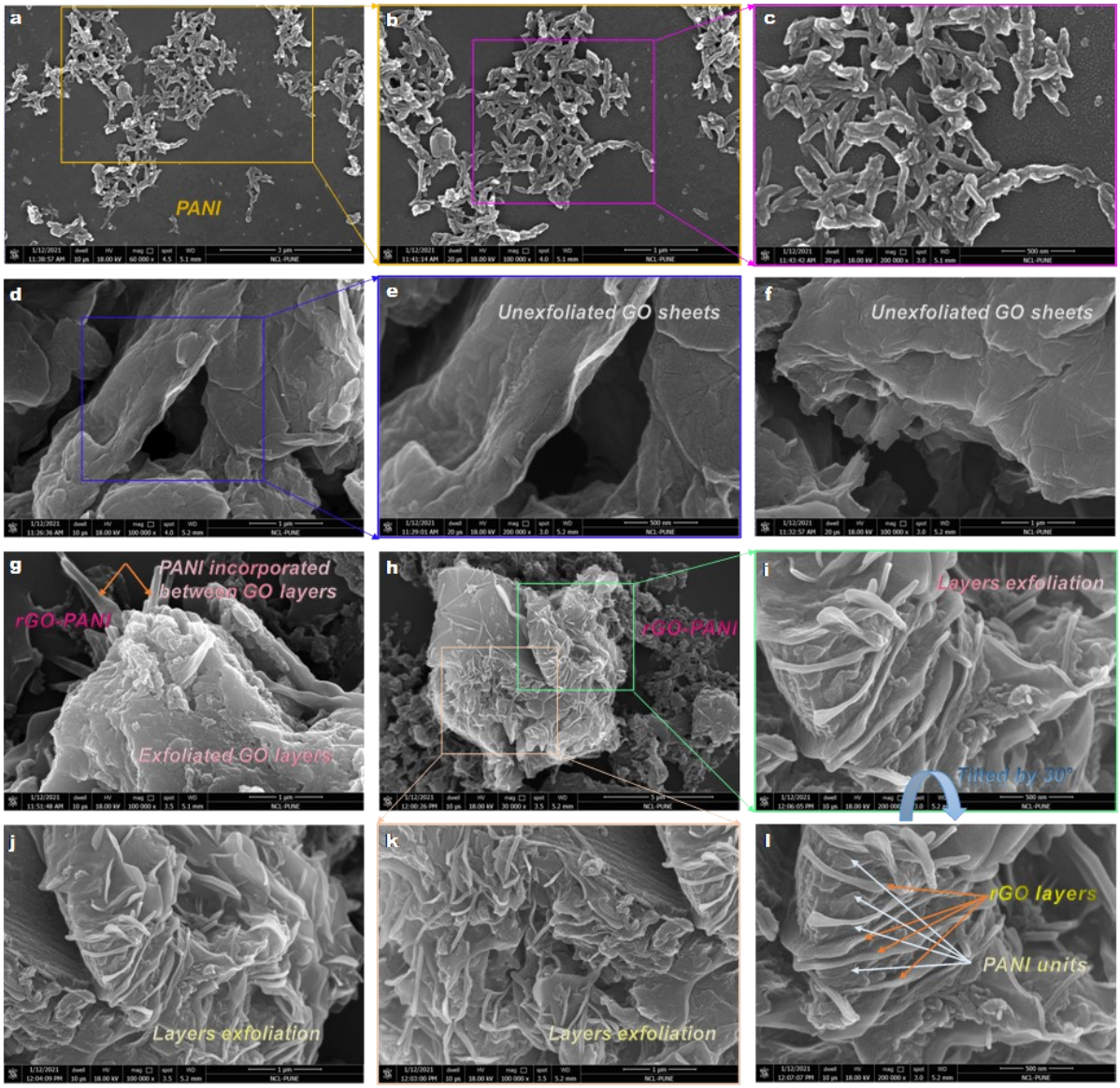

Fig. S8. Field emission scanning electron microscope (FE-SEM) analysis of GO, PANI and rGO-PANI

Field emission scanning electron microscopy (FE-SEM) images of pristine polyaniline (PANI) reveal a well-defined nanobelt-like morphology (a–c).(d–f) FE-SEM micrographs of pristine graphene oxide (GO) display unexfoliated sheet-like structures. (g–i) Micro/nanographs of the rGO–PANI composite clearly show the incorporation of PANI nanobelts between reduced graphene oxide (rGO) layers (g). This intercalated morphology is consistently observed across different regions of the sample (h). (i–k) For deeper structural

insight, the rectangular region highlighted in (h) was magnified, and the sample stage was tilted by 30° at the region shown in (i), yielding enhanced visualization of the interlayer arrangement (i, j, l). These observations support the proposed structure of rGO–PANI, wherein PANI units are tightly embedded between rGO layers, likely via covalent (-C–N-) bonding.

Thermal stability of rGO-PANI

To evaluate the thermal stability of pristine GO, PANI, and the rGO–PANI composite, thermogravimetric analysis (TGA) was conducted using a PerkinElmer STA 6000 instrument over a temperature range of 50–900 °C at a heating rate of 10 °C min^{-1} under a nitrogen atmosphere. The corresponding thermograms are presented in **Figure S9 a–c**.

The TGA profile of pristine GO (**Figure S9a**) exhibits an initial weight loss of 11.8% between 100–125 °C, attributed to the evaporation of physically adsorbed water. A further 15% weight loss below 200 °C corresponds to the decomposition of labile oxygen-containing groups such as carbonyl and carboxyl, releasing CO and CO_2. A significant weight loss of 23.9% between 200–260 °C is assigned to the removal of epoxy and hydroxyl groups. Above 300 °C, the weight loss decreases gradually, indicating the onset of GO reduction and the formation of rGO [29].

The TGA curve for pristine PANI (**Figure S9b**) shows three distinct weight loss events. The first, a 5.0% loss between 80–100 °C, arises from the desorption of water and volatile impurities. The second stage, accounting for 67.4% weight loss between 250–310 °C, is attributed to the elimination of Cl^- dopants. The third stage, with a 10.13% weight loss from 420–520 °C, corresponds to the thermal decomposition of the PANI backbone [28].

Interestingly, the rGO–PANI composite (**Figure S9c**) displays a two-step weight loss process. The first stage, a 5.3% loss between 85–100 °C, is ascribed to the removal of residual water and volatiles, comparable to pristine PANI and significantly lower than in GO.

The second stage shows only a 24.5% weight loss between 290–400 °C, approximately threefold lower than the corresponding degradation in pristine PANI.

This reduced thermal degradation in rGO–PANI strongly suggests the formation of a more stable network, likely due to covalent linkage (–C–N–) between PANI chains and the rGO sheets. These findings indicate that the rGO–PANI composite exhibits enhanced thermal stability compared to both pristine GO and PANI.

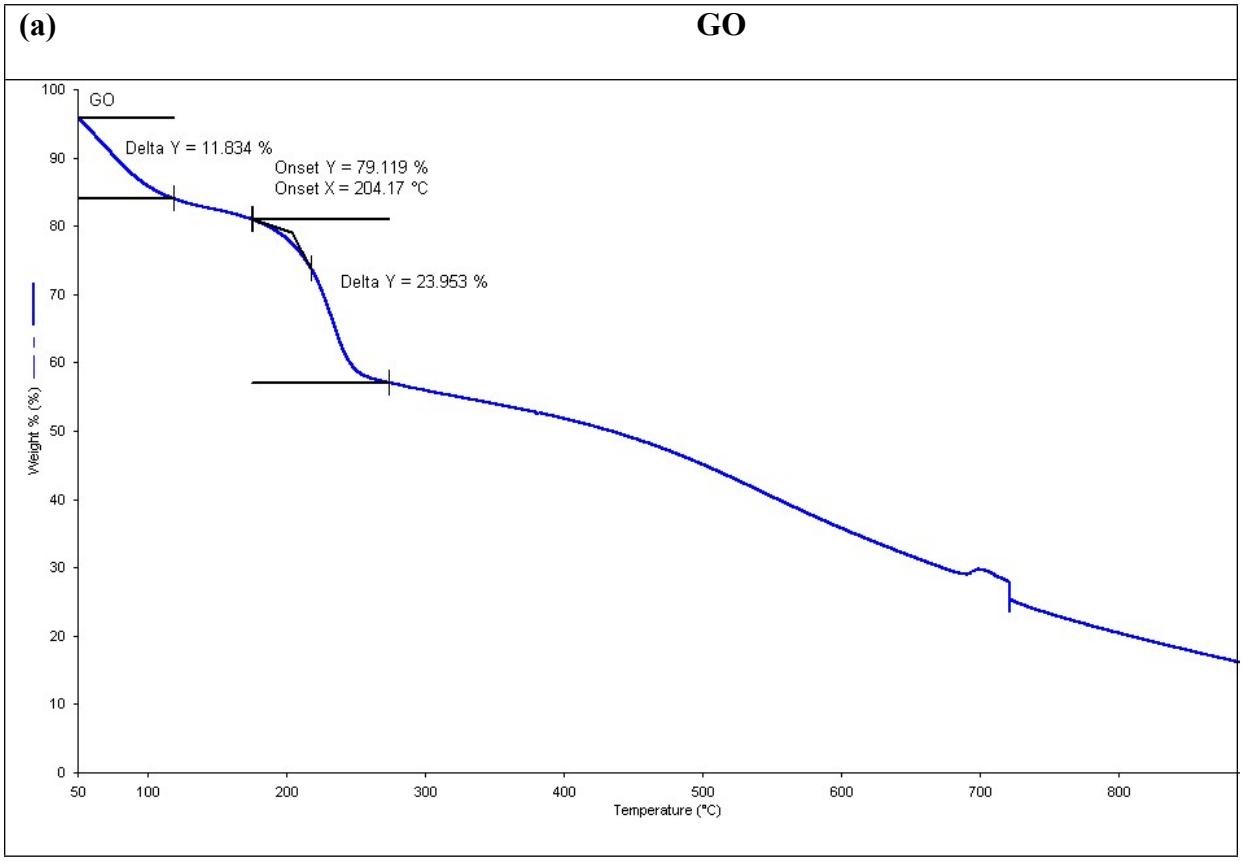

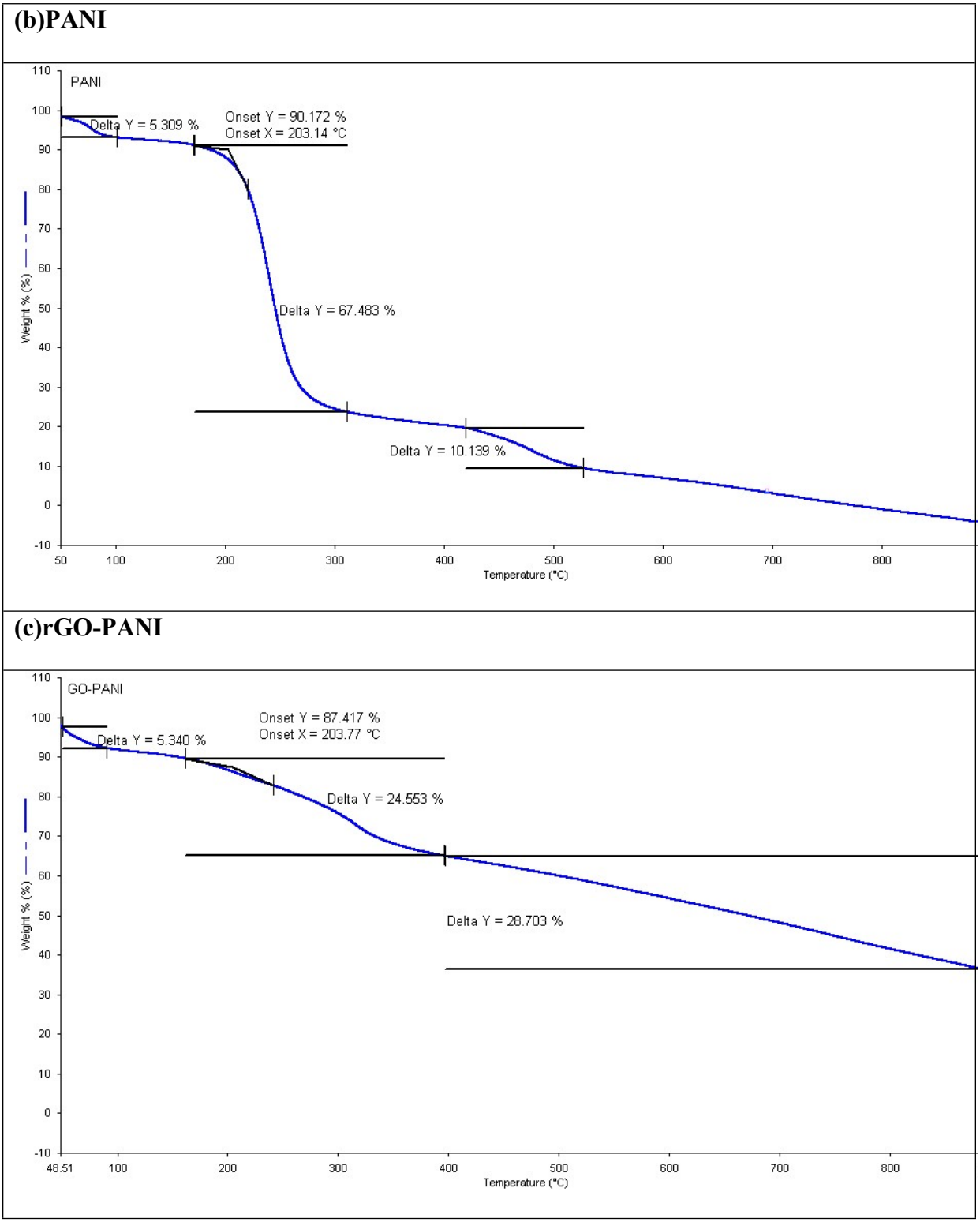

Fig. S9. Thermogravimetric analysis (TGA) curve of GO, PANI, and rGO-PANI, shown in Fig. S9(a), (b), and (c), respectively.

Detailed analysis of plausible formation of rGO-PANI (RGyOP): Detailed understanding of the proposed mechanistic pathway for the plausible formation of rGO-PANI in **Scheme S4-S10,**through the reactions A (Basal dehydro-deprotonation of GO), B (Nucleophilic attack via S_N2 to the basal epoxide rings opening of the GO along with simultaneous polymerisation of aniline hydrochloride) and C (Edge decarboxylation of GO). These reactions are probed by considering the reaction conditions with the individual reactants along with complementary experimental results as depicted in reaction **Schemes**steps**S4 to S10**). The reaction **Scheme**steps**S4-I** to **S4-III** indicates the protonation of basal hydroxyl groups of the GO (in DMSO), which is initiated by the addition of HCl. The reaction follows general mechanism of protonation at hydroxyl groups leading to the formation of alkyloxonium ion (step **S4-I**). The alkyloxonium ion spontaneously undergoes dehydration reaction with simultaneous deprotonation reaction resulting in additional sp^2 centres (step **S4-II** and **S4-III**) leading to enhancement in conjugation. The enhanced conjugation is confirmed by Baeyer's test of the GO as color changed is observed (**Scheme 4**).

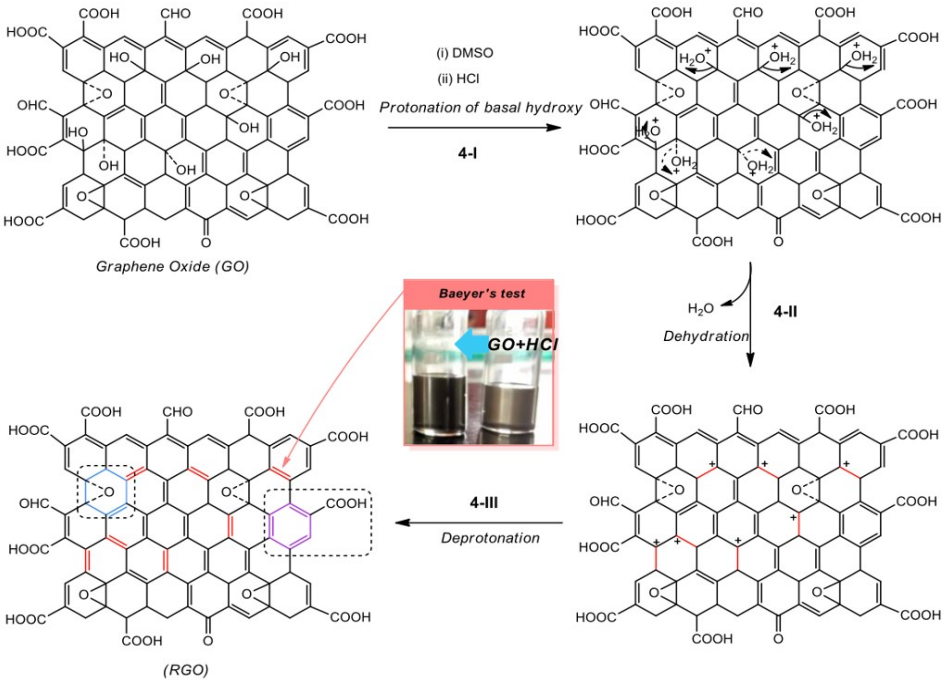

Scheme S4. Basal dehydro-deprotonation of GO to form rGO.

The resulting modified GO[reduced graphene oxide (rGO) undergoes simultaneous reaction at basal and edge side of rGO as shown in reaction **Scheme S4**. Each of these reaction steps are illustrated below:

Simultaneous reactions:

(I) Basal epoxide opening reaction and aniline monomer polymerization: For ease of understanding the reaction is represented considering single component of GO with epoxide ring, where aniline monomer initiates a nucleophilic attack on the epoxide ring opening reaction via back side (BS) attack by S_N2 mechanism generating a covalent bond between rGO and aniline monomer. The epoxide ring opening give rise to formation of new hydroxyl groups in adjacent carbon where nitrogen is attached as shown in Steps **(5-I)** to **(5-II)**.

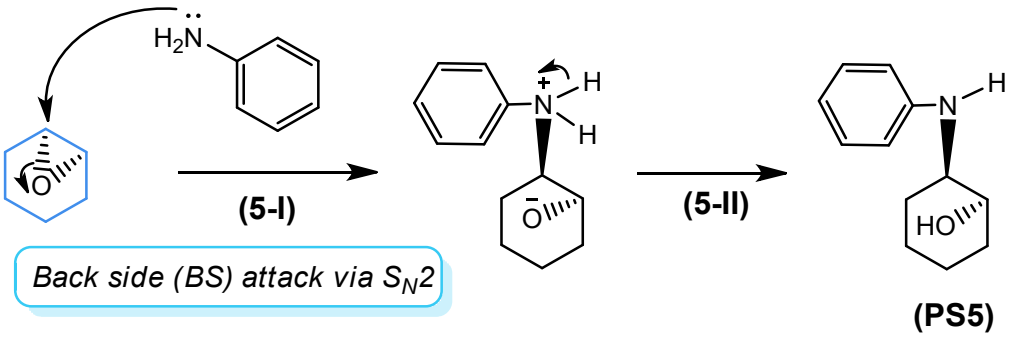

Scheme S5.GObasal epoxide ring opening reaction via aniline monomer.

Upon addition of APS (**Scheme S6**step 6-**I** to **6-III**), itreacts with product of **Scheme 5** (**PS5**) in the reaction mixture. A cyclic transition state (CTS) is proposed through step (**6-I**) and (**6-II**) [30].The CTS undergoes elimination reaction in the form of mono hydrogen sulphate radical which is consistent with the reported polymerization reaction of ammonium persulfate/aliphatic diamine systems as initiator [31], resulting in a nitrogen centred radicalwhich acts as initiator of the polymerization reaction with another aniline monomer in

parallel with normal polymerization by APS via deprotonation step (**6-III**). The reaction steps (**6-I**) to (**6-III**) leads to the formation of polyaniline and RGO bonding (blue color) through -C-N- bond and creation of new -OH (purple color) functional groups on rGO.

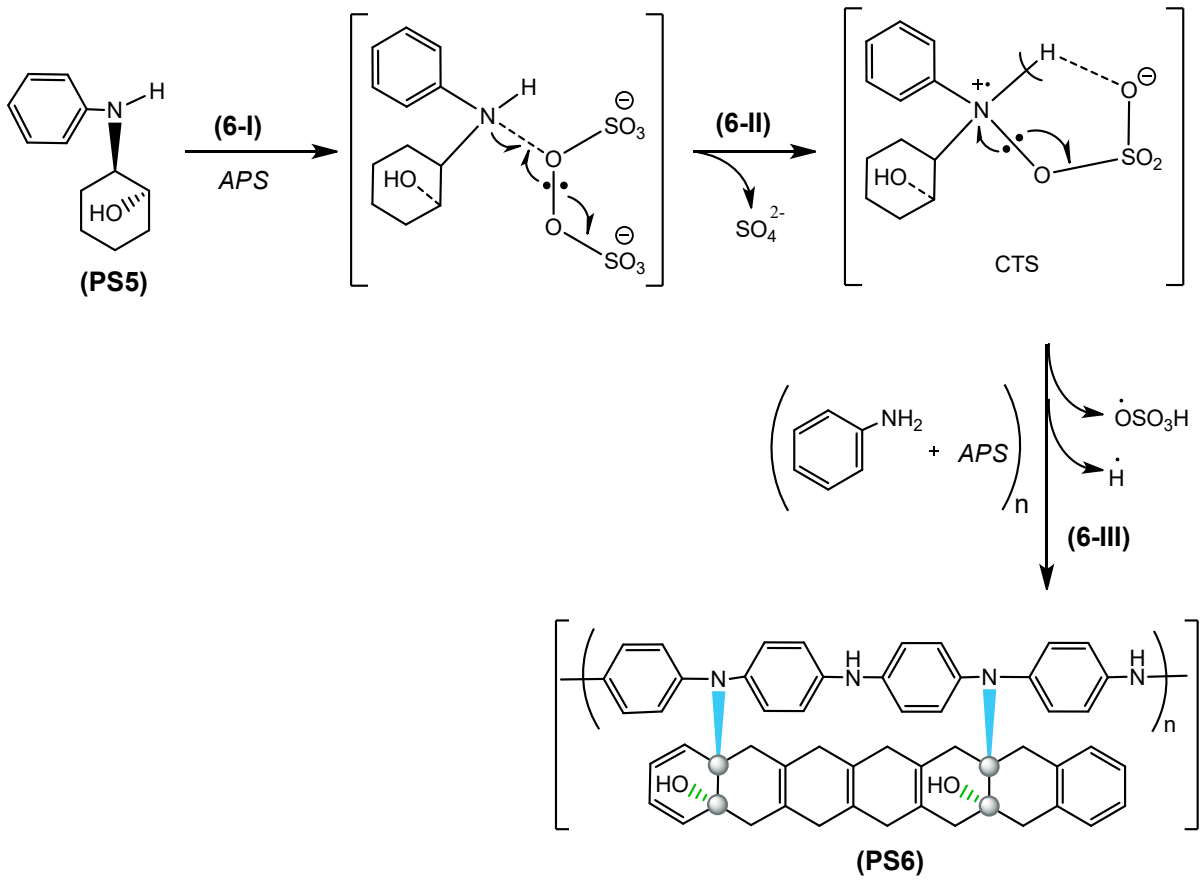

Scheme S6.rGObasal epoxide ring opening reaction via aniline monomer.

(II) Edge side reaction (Edge decarboxylation of rGO): As we know that benzoic acid type (BAT) moiety (with free ortho positions) exists in rGO edges side. The conversion of BAT moiety into ortho chloro-BAT directly is not feasible in the presence of HCl, as it does not react with BAT as represented in **Scheme S7**.

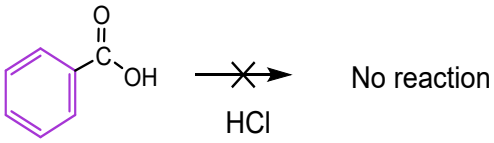

Scheme S7. Benzoic acid type (BAT) moiety in rGOedges does not react with HCl to give orthochloro benzoic acid.

As reported, the reaction of orthochloro benzoic acid with aniline in presence of base or K_2CO_3/CuO to form a N-phenyl anthranilic acid [32,33] Such intermediate formation is proposed in the rGO edge side reaction conditions as depicted in **Scheme. S8**.

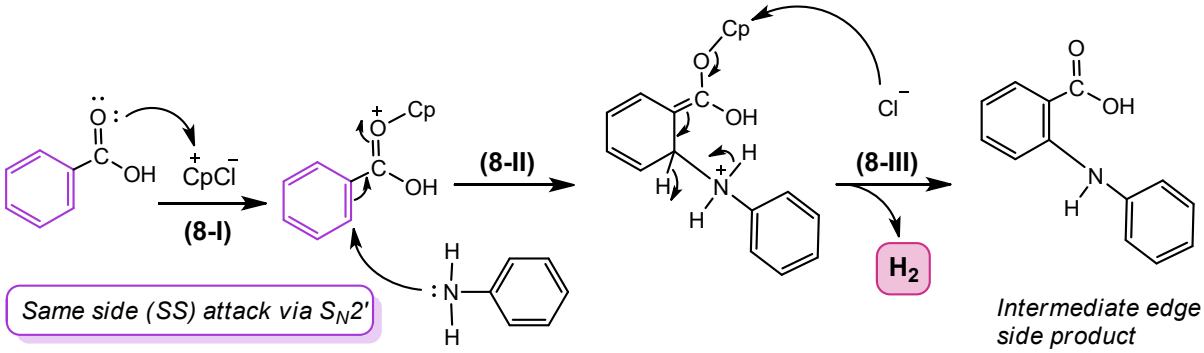

Scheme S8. Proposed**r**GOedge side reaction via aniline nucleophile in presence of CpCl.

Although, we believed that the hypotheses reaction steps occurred in our complex reaction mixture as shown in **Scheme. S8**, there is no direct evidence of **Scheme. S8** reported so far. Therefore, to validate this hypothesis reaction steps (**Scheme. S8-I** to **S8-III**), we performed a controlled experiment via addition of aniline and HCl in GO solution in presence of surfactant CpCl.This led to the evolution of H_2 in reaction mixture as confirmed by gas chromatography (GC) experiment (**Fig. S11a**) complementing the proposed reaction step **Scheme S8-III**, via a nucleophile attack on the ortho position of the rGO edge carboxylic groups through the same side in a S_N^2 fashion. The cationic part (Cp^+) of ionic salt (CpCl) acts as an electrophile, attacking the carbonyl oxygen of BAT moiety to form oxonium ion as shown in reaction step **Scheme. S8-I**.Additionally, we performed another set of reaction to check the formation of intermediate edge side product (N-phenyl anthranilic acid) via reaction of benzoic acid with aniline in presence of CpCl (in water). The product was

successfully extracted in benzene (**see details in sectionS2.1.5**). The N-phenyl anthranilic acid derivative product formation was confirmed by ^{1}H, ^{13}C NMR and HRMS (**Figure S11b-d**).

Further N-phenyl anthranilic acid type moiety (edge side intermediate product) undergoes polymerization reaction with ammonium persulphate (APS) as reported by Ozkan et al at different reaction conditions [34]. But in the proposed hypothesis, APS addition leads to the formation of contact-charge-transfer (CCT) complex as shown in reaction step **Scheme S9-I.** [35]The CCT complex eliminates sulphate ions to form a quaternary ammonia salt (QAS) via reaction step **SchemeS9-II** leading to a cyclic transition state (CTS) as shown in reaction step **Scheme S9-III [36].** The CTS further undergoes elimination reaction of mono hydrogen sulphate radicals via deprotonation as shown in reaction step **Scheme S9-IV,**followed by decarboxylation illustrated in reaction step **Scheme S9-V** which finally leads to the formation of benzyne [37-38]with acetylenic or sp-sp^2carbons (-C≡C-) in the rGO edges which is termed as reduced graphyne oxide (RGyO). These sp-sp^2carbons on the edges along with sp^2 carbons are characteristics of graphyne [39-26].

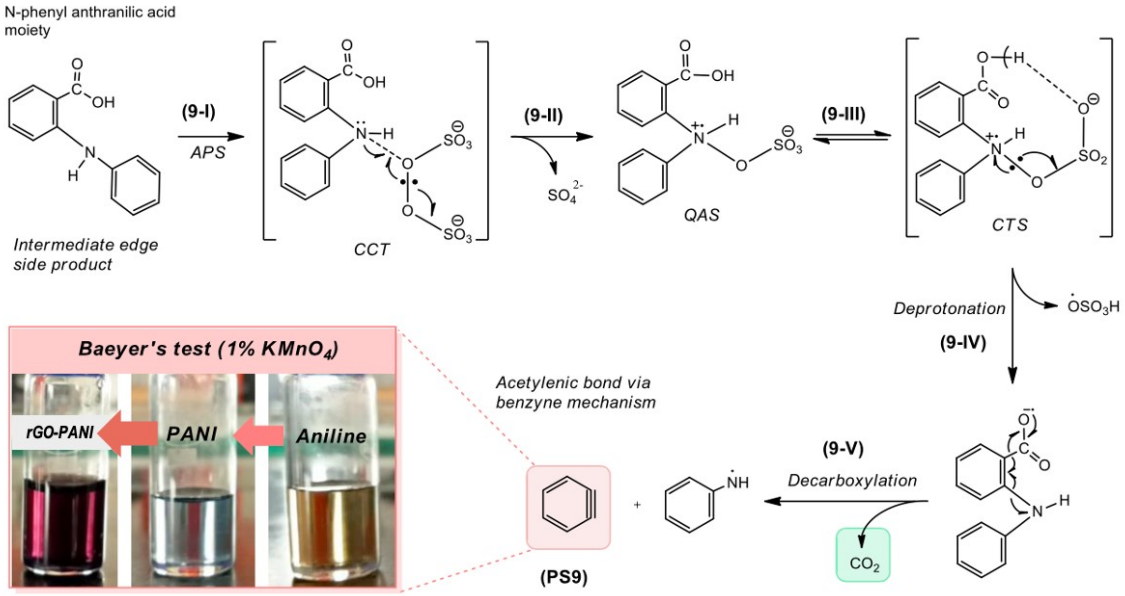

Scheme S9. Acetylenic bond (sp-sp^2) formation through polymerization of rGO edge side intermediate product (N-phenyl anthranilic acid type moiety) leading to formation of rGO.

The enhanced conjugation via formation of graphyne (-C≡C-) edges in rGO sheet arises due to the removal of CO_2 because of the elimination reaction of COOH groups, which was verified by performing a Baeyer's test. This shows the change in color (**Scheme S9**). Further CO_2 evolution was confirmed by GC experiment (**Figure S11e**and repeated experiment shown in **Figure S11f**) as well as a real-time observation of colored water test was performed after completion of reaction. This is based on the trapped molecules of CO_2 into lamellar mesophase which creates a suction pressure to draw in the colored water (**FigureS11g**).

Further, addition of co-surfactant '1-pentanol' with adjusted amount in hexagonal mesophase decreases the surface tension of the hexagonal cylinder leading to unzipping of the hexagonal cylinders to 2D lamellar mesophase. 1-pentanol also act as a crosslinker in the aniline polymerization reaction [37].Therefore, '1-pentanol' addition led to the crosslinking in the polymeric chain of aniline (PS6) as a result of basal plane reaction followed by reaction step

Scheme S10-Iand acetylenic bonds (PS9 as a result of edge side reaction)via reaction step **Scheme S10-II**are formed. The 2D-2D interaction between aniline polymeric chain and reduced graphyne oxide leads to plausible formation of reduced graphyne oxide polyaniline (RGyOP) as shown in **Scheme S10**.

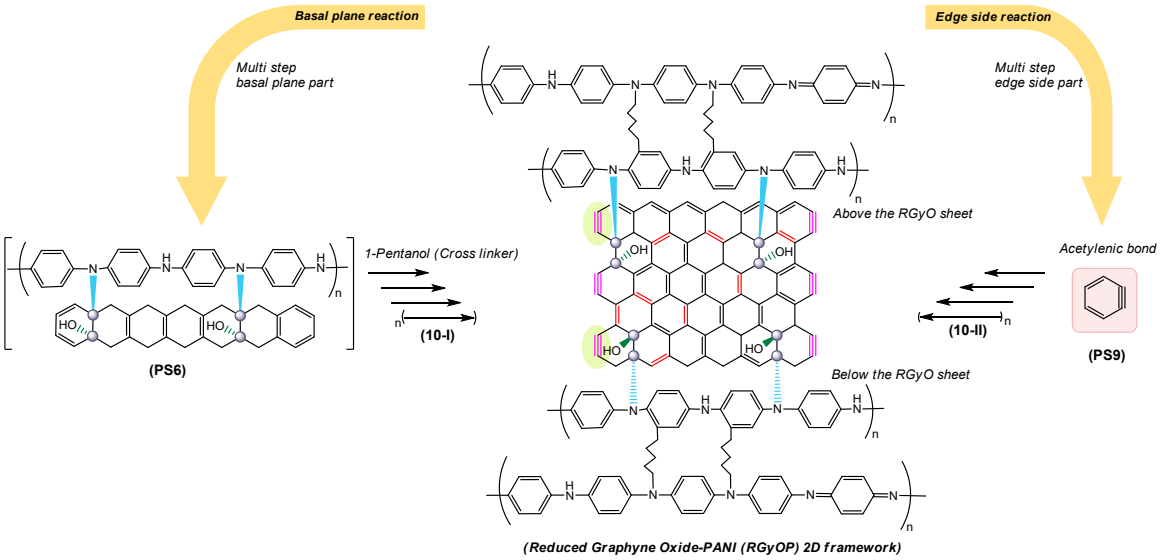

Scheme S10. Formation of final product rGO-PANI via simultaneous basal and edge side reactions of GO with aniline monomer.

Detection of H_2, CO_2 evolution and intermediate for the formation of rGO-PANI:

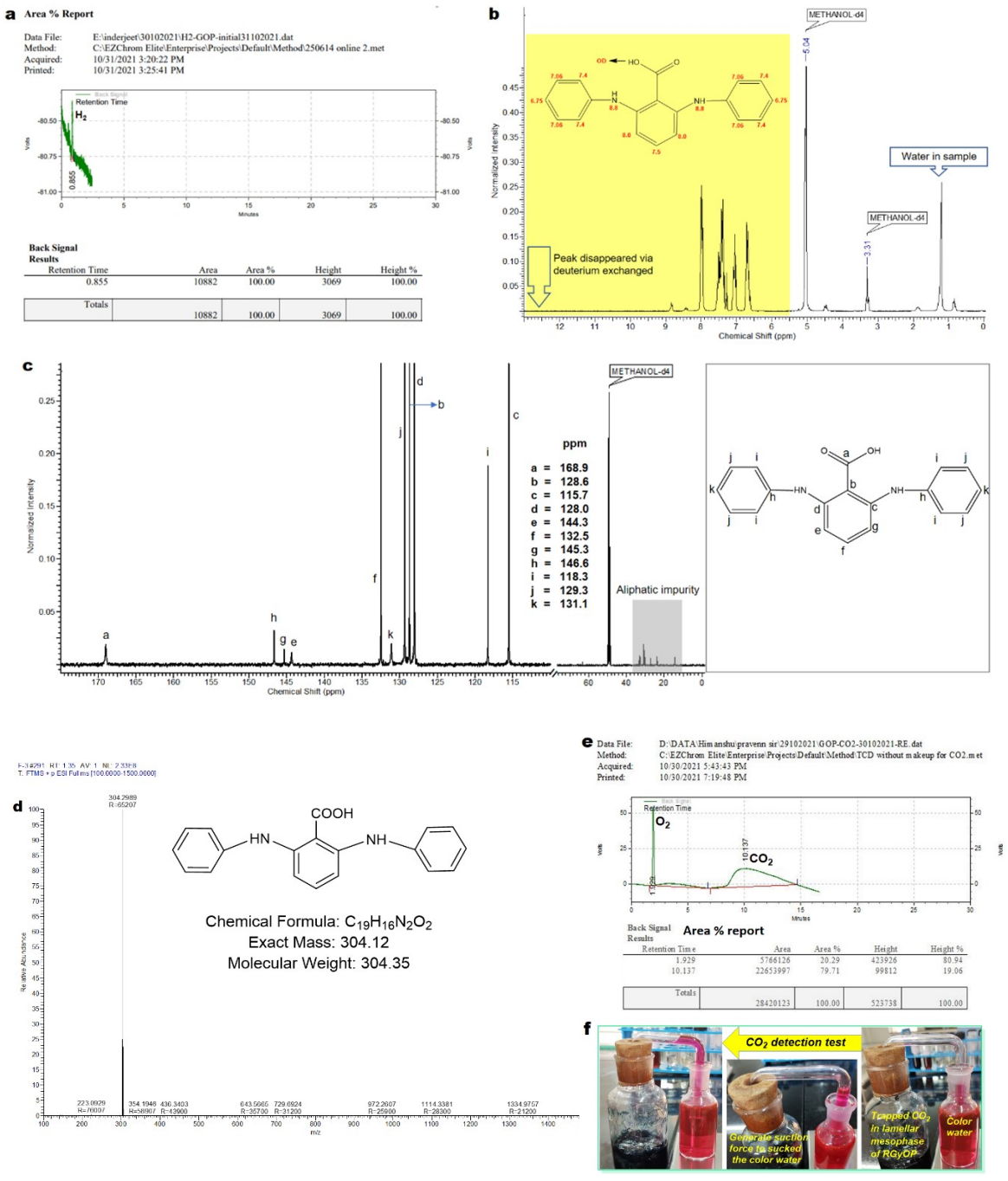

Fig. S10. Detection of H_2, CO_2 evolution and intermediate product analysis:**(a)**time *vs* volts graph of gaseous species H_2 evolved during the rGO-PANI (RGyOP) formation; (**b-d)**^{1}H, ^{13}C NMR and HRMS analysis of synthesized derivative ofN-phenyl anthranilic acid as an edge-side intermediate product; (**e)** CO_2 detection via GC experiments which evolved during the RGyOP formation; (**f)**colored water test of CO_2 detection.

Stability of rGO-PANImodified GCE electrode against glucose sensing

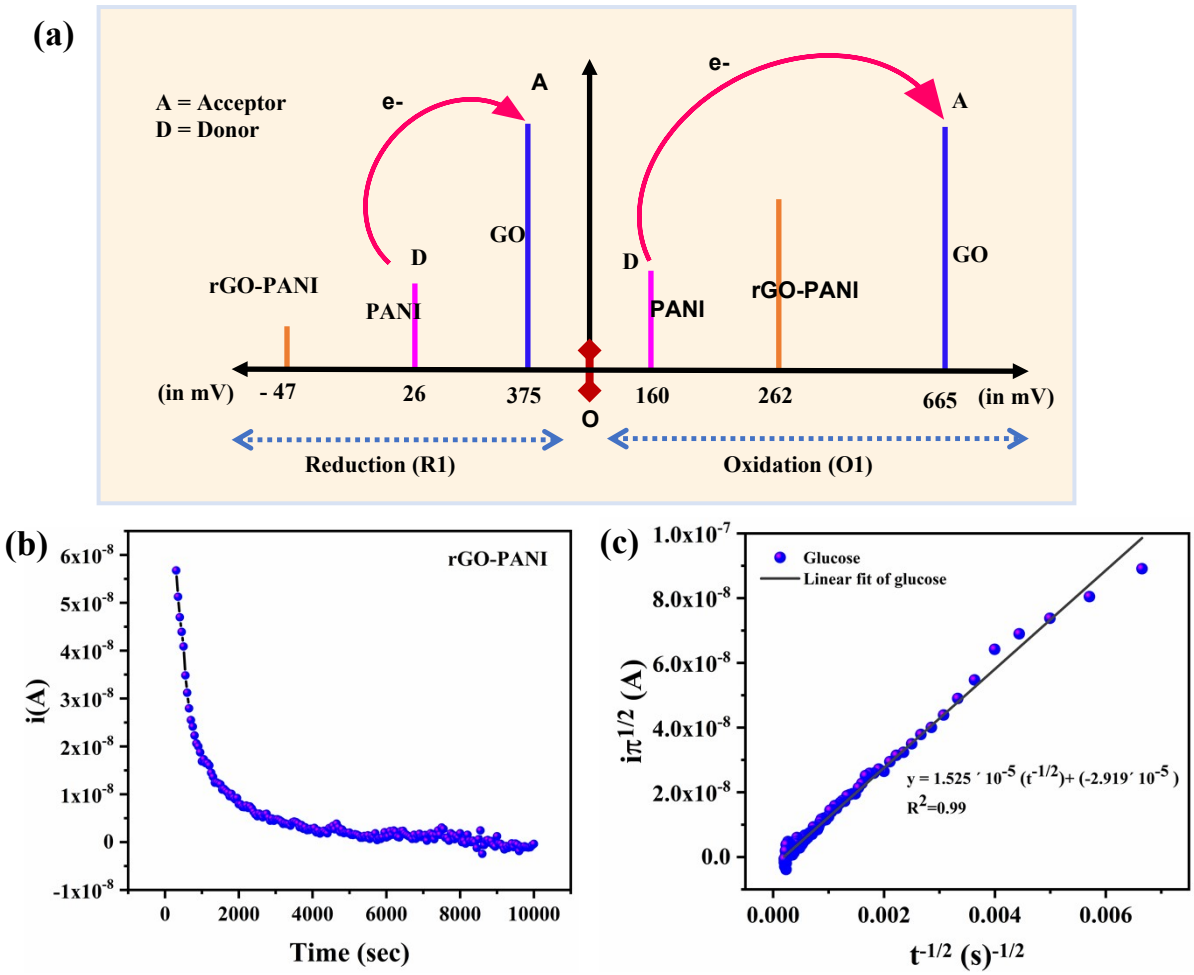

Fig. S11.(a) Chart for the potential shift in glucose oxidation (O_1, O_2) and reduction (R_1, R_2) occurs at GCE electrode modified by GO, PANI and rGO-PANI. (b) Stability of rGO-PANI/GCE modified electrode analysed by chronoamperometry measurement at constant potential (50 mV) for 10000 s. (c) Cottrell plot obtained from chronoamperometric measurements conducted in 0.1 M acetate buffer (pH 7.4) containing 0.2 nM glucose.

Mechanistic study of electron transfer through HOMO-LUMO between the analyte molecule and rGO-PANI

The mechanism underlying electron transfer between the rGO–PANI heterostructure and glucose molecules is elucidated through a proposed energy level diagram based on experimentally determined HOMO–LUMO positions (**Figure S12a–c**). Electrochemical

analysis reveals that the HOMO level of PANI (−4.7 eV) lies above that of GO and rGO–PANI (−0.48 eV), while the LUMO levels are aligned at −4.0 eV (**Figure S12a**). Under these conditions, hole generation occurs at the HOMO of PANI, while electrons excited to its LUMO are transferred to the LUMO of rGO–PANI, facilitating oxidation of glucose at the rGO–PANI–modified GCE interface. This interfacial charge transfer mechanism is schematically depicted in **Fig. S12b**, with the electron pathway further visualized in the proposed model in **Fig. S12c**.The electron transfer path between glucose molecule and rGO-PANI is further analysed via proposed mechanism as illustrated in **Fig. S12c**.In step (I), D-glucose undergoes an initial oxidation at the electrode surface, corresponding to the broad anodic peak O1, with the simultaneous loss of one electron and one proton, forming glucose radical. This is a slow step characterized by a high activation energy (Ea) and a low electron transfer rate constant ($k = 2.48 \times 10^3$ cm^{-1})[40].In step (II), the glucose radical is rapidly converted to gluconolactone through the loss of an additional electron and proton (peak O2), representing a fast step with a lower Ea and higher rate constant ($k = 30.58 \times 10^3$ cm^{-1}). Step (III) involves the reduction of gluconolactone via radical formation, as evidenced by the sharp cathodicpeak R2. This is also a fast step ($k = 26.24 \times 10^3$ cm^{-1}). In step (IV), the gluconolactone radical is reduced to its final form through the gain of one electron and one proton (peak R1), which is comparatively slower ($k = 9.13 \times 10^3$ cm^{-1}) due to a higher Ea. The correlation between the activation energies and rate constants confirms the kinetic hierarchy of the redox events, reflected in the sharpness and broadness of the CV peaks (O1-broad, O2-sharp, R2-sharp, R1-broad).

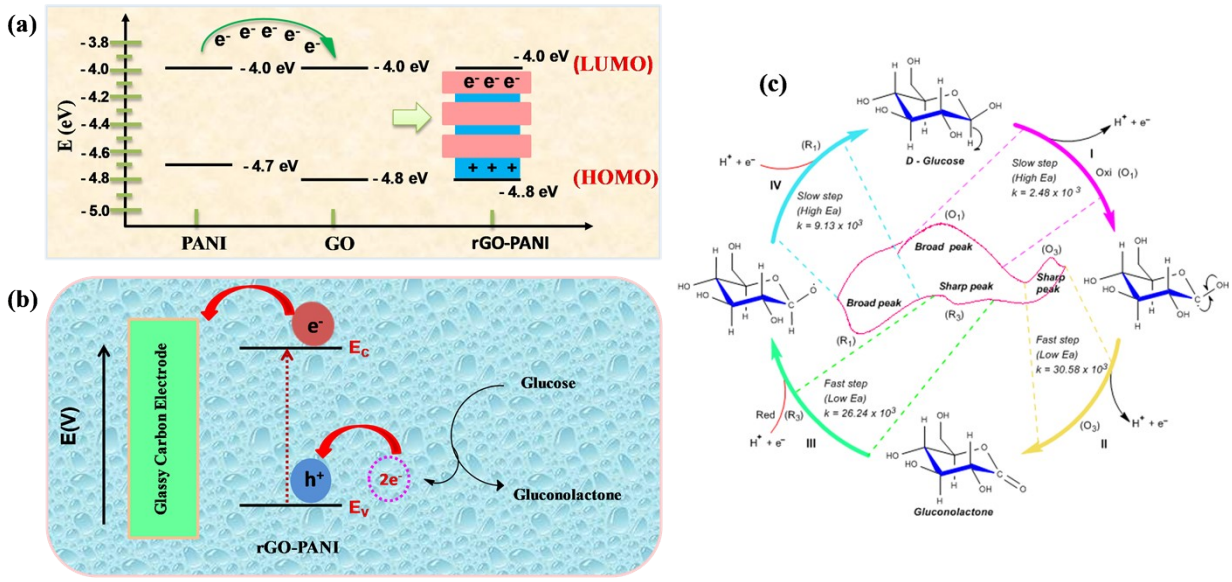

Fig. S12. Mechanistic insights into glucose oxidation at the rGO–PANI interface. (a) Experimentally observed vacuum-corrected energy level diagram showing HOMO and LUMO positions of GO, PANI, and the rGO–PANI heterostructure. (b) Schematic representation of glucose oxidation on a glassy carbon electrode (GCE) modified with rGO–PANI. (c) Proposed stepwise mechanism of glucose oxidation via proton-coupled electron transfer, illustrating the sequence of redox events observed in cyclic voltammetry (CV).

Table S1. Comparison table for glucose sensing with literature reports

Cu based Metal nanocomposite					
Material (Electrode)	**Potential (V)**	**Sensitivity ($\mu A\ mM^{-1}\ cm^{-2}$)**	**Linear Range (mM)**	**LOD (µM)**	**Ref.**
CuCo-CFs/Nafion/GC	+6	-	0.02-11	1	[41]
Cu based Carboneous Metal/ Metal Oxide nanocomposite					
CuO-G-CGE	+0.59	1360	0.002-4	0.7	[42]
CuNT/MWCNT	+0.65	1096	5-7.5	1	[43]
Nickel based Carbeneous Metal/Metal Oxide nanocomposite					
rGO-$Ni(OH)_2$/GCE	-	-	0.002-3.1	0.6	[44]
Cs-rGO-NiNPs/SPE	-	318.4	0.2- 9.0	4.1	[45]

NA/NiONF-rGO/GCE	-	1100	0.002-0.60	0.77	[46]
Carbaneous /Metal based nanocomposite					
Silver/silver oxide /RGO	+0.60	32	0.2-8	60	[47]
GR-Nafion/Pd NPs/GCE	+65	-	0.01- 5.0	1	[48]
AuNP/NG-modified ITO	+35	-	0.04-16.1	12	[49]
Conducting polymer/Metal based nanocomposite					
GCE/GNPs/GOD / CNT/pv	-	-	0.5-8	200	[50]
GCE/PANI/GNPs/cyt/GOD	-	-	0.01-5.0	10	[51]
AuNPs - graphene/ILE	-	978116.3	-	0.062/ 0.183	[52]
Metal based nanocomposite					
3D hierarchical porous Au networks	+1	-	0.001 – 0.5& 0.01-7.5	0.2	[53]
Pt/Au/BDD electrode	-0.15	-	4.0 - 12	6	[54]
Conducting Polymer based nanocomposite					
GOX-graphene -CGE	-0.40	110	0.1-10	10	[55]
Cellulose/MWCNT/GOX/GCE	-	6.57	0.05-1	-	[56]
rGO-PANI/GCE	+7	372660	55.4×10^{-8} - 1×10^{-6}	50×10^{-6}	**This work**

References

[1]. D.C. Marcano, D.V. Kosynkin, J.M. Berlin, A Sinitskii, Z. Sun, A. Slesarev, L. B. Alemany, W. Lu, and J.M. Tour, ACS nano,2010, 4,4806-4814.

[2]. K. J. Kshirasagar, U. S. Markad, A. Saha, K. K. K. Sharma, G. K. Sharma, Materials Research Express,2017, 4,025015.

[3] H. Chang, H. Wu, Energy Environmental Science,2013, 6,3483-3507.

[4] Q. Li, X. Li, S. Wageh, A. A. Al-Ghamdi, J. Yu, Advanced Energy Materials, 2015, 5,1500010.

[5] N. A. Kumar, H.-J. Choi, Y. R. Shin, D. W. Chang, L. Dai, J.-B. Baek, ACS Nano,2012, 6,1715-1723.

[6] X. Chang, M. F. El-Kady, A. Huang, C. W. Lin, S. Aguilar, M. Anderson, J. Z. J. Zhu, R. B. Kaner, Advanced Functional Materials, 2021,31,2102397.

[7] C. Wang, Y. Yang, R. Li, D. Wu, Y. Qin, Y. Kong, Chemical Communications, 2020,56,4003-4006.

[8] L. Wang, X. Lu, S. Lei, Y. Song, Journal of Materials Chemistry A, 2014,2,4491-4509.

[9] H. Chang, H. Wu, Energy Environmental Science, 2013,6,3483-3507.

[10] Q. Wu, Y. Xu, Z. Yao, A. Liu, G. Shi,ACS Nano,2010, 4,1963-1970.

[11] Y. Wang, S. Wang, P. Li, S. Rajendran, Z. Xu, S. Liu, F. Guo, Y. He, Z. Li, Z. Xu, Matter, 2020, 3, 230-245.

[12] P. D. Pancharatna, G. Jhaa, M. M. Balakrishnarajan, The Journal of Physical Chemistry C, 2019, 124, 1695-170.

[13] I. Jung, D. A. Field, N. J. Clark, Y. Zhu, D. Yang, R. D. Piner, S. Stankovich, D. A. Dikin, H. Geisler, C. A. Ventrice Jr, The Journal of Physical Chemistry C, 2009,113, 18480-18486.

[14] C. K. Chua, M, Pumera. ACS Nano, 2015,9,4193-4199.

[15] D. Dambournet, I. Belharouak, J. Ma, K. Amine,Journal of Power Sources, 2011, 1962871-2874.

[16] T. Zhou, F. Li, Y. Fan, W. Song, X. Mu, H. Zhang, Y. Wang, Chemical communications, 2009, 22,3199-3201.

[17] H. S. Magar, R. Y. Hassan, A. Mulchandani, Sensors,2021, 21, 6578.

[18] P. Kumar, H. Bajpai, C. S. Gopinath, M. N. Luwang, Inorganic Chemistry. Inorganic Chemistry, 2021,61,279-286.

[19] Q.Tang, C. Zhang, M. A. Luo, Journal of the American Chemical Society, 2008,130,5840-5841.

[20] J. Li, X. Zhang, Z. Zhang, P. K. Padakanti, H. Jin, J.Cui, A. Li, D. Zeng, N.P. Rath, H. Flores, and J.S. Perlmutter, Journal of medicinal chemistry, 2013,56,6216-6233.

[21] E. Boess, C. Schmitz, M. A. Klussmann, Journal of the American Chemical Society,2012, 134, 5317-5325.

[22] C. Fulton, G. Lucovsky, R Nemanich, Journal of applied physics, 2006,99,063708.

[23] Y. Fang, Y. Xue, Y. Li, H. Yu, L. Hui, Y. Liu, C. Xing, C. Zhang, D. Zhang, Z.Wang, and X. Chen, Angewandte Chemie International Edition, 2020,59,13021-13027.

[24] X. Liu, S.M. Cho, S. Lin, E.Yun, E.H. Baek, Z. Chen, D.H. Ryu, and H. Lee, arXiv preprint arXiv, 2019,1907,03534.

[25] J. Guo, M. Guo, F.Wang, W. Jin, C. Chen, H. Liu, and Y. Li,Angewandte Chemie International Edition, 2020,59,16712-16716.

[26] H. Bao, L.Wang, C. Li, & J. Luo, ACS applied materials interfaces, 2018,11, 2717-2729.

[27] L. Li, L. Qin, X. Fan, X. Li, & M. Deng, Frontiers of Materials Science, 2021,15147-157.

[28] H. Peng, Z. Mo, S. Liao, H. Liang, L.Yang, F. Luo, H. Song, Y. Zhong, Zhang, B, Scientific reports,2013, 3,1-7.

[29] H. Yang, C.Shan, F. Li, D. Han, Q. Zhang, L. Niu, Chemical Communications,2009, 26,3880-3882.

[30] X. Q. Guo, K. Y.Qiu, X. De Feng, Macromolecular Chemistry Physics, 1990,19,577-587.

[31] K. Si, X. Q Guo, K. Y.Qiu, Journal of Macromolecular Science Part A,1995, 32,1149-1159.

[32] T. Zhou, F. Li, Y. Fan, W. Song, X. Mu, H. Zhang, Y.Wang,Chemical communications,2009, 22, 3199-3201.

[33] B. Bhudevi, P. V. Ramana, A. Mudiraj, A. R. Reddy, Indian Journal of Chemistry, 2009.

[34] S. Z.Ozkan, I. S. Eremeev, G. P. Karpacheva, G. N. Bondarenko, Open Journal of Polymer Chemistry, 2013,3,63-69.

[35] X. Q.Guo, K. Y. Qiu, X. De Feng, Macromolecular Chemistry Physics,19990, 191, 577-587.

[36] J. D. Roberts,Chemical Society, 1958, 115,115-130.

[37] M. Panar, J. D. Roberts,Journal of the American Chemical Society, 1960,82, 3629-3632.

[38] X. Gao, H. Liu, D. Wang, & J. Zhang, Chemical Society Reviews, 2019,48,908-936.

[39] J. Chen, Y. Ao, T. Lin, X.Yang, J. Peng, W. Huang, J. Li, and M. Zhai, Polymer journal, 2016, 87,73-80.

[40]. J. Chen, Y. Ao, T. Lin, X.Yang, J. Peng, W. Huang, J. Li, M. Zhai, Polymer, 2016,87,73-80.

[41] M. Li, L. Liu, Y. Xiong, X. Liu, A. Nsabimana, X. Bo, L. Guo, Sensors Actuators B: Chemical, 2015,207,614-622.

[42] L. Luo, L. Zhu, Z. Wang, Bioelectrochemistry,2012, 88,156-163.

[43] J. W. Yang, D. Zhang, S. Gunasekaran, Biosensors Bioelectronics,2010, 26,279-284.

[44] Y. Zhang, F. Xu, Y. Sun, Y. Shi, Z. Wen, Z. Li. Journal of Materials Chemistry,2011, 21,16949-16954.

[45] J. Yang, J.H.Yu, J. R. Strickler, W.J. Chang, S. Gunasekaran, Biosensors Bioelectronics,2013, 47, 530-538.

[46] Y. Zhang, Y. Wang, J. Jia, J. Wang, Sensors Actuators B: Chemical,2012, 171,580-587.

[47] L. Shahriary, A. A. Athawale, Journal of Solid State Electrochemistry,2015, 19,2255-2263.

[48] L. M. Lu, H.B. Li, F. Qu, X. B. Zhang, G. L.Shen, R.Q. Yu,Biosensors Bioelectronics,2011, 26,3500-3504.

[49] T. D.Thanh, J. Balamurugan, S. H. Lee, N. H. Kim, J. H. Lee, Biosensors Bioelectronics,2016, 81,259-267.

[50] H. Zhang, Z. Meng, Q. Wang, J. Zheng, Sensors Actuators B: Chemical, 2011,158,23-27.

[51] C. Xiang, Y. Zou, S. Qiu, L. Sun, F. Xu, and H. Zhou,Talanta,2013, 110,96-100.

[52] J.W.Wu, C. H. Wang, Y.C.Wang, J. K. Chang, Biosensors Bioelectronics, 2013,46,30-36.

[53] S.L. Zhong, J. Zhuang, D. P. Yang, D. Tang, Biosensors Bioelectronics,2017, 96,26-32,

[54] S. Nantaphol, T. Watanabe, N.Nomura, W.Siangproh, O.Chailapakul, and Y. Einaga, Biosensors Bioelectronics,2017, 98,76-82.

[55] P.Wu, Q. Shao, Y. Hu, J. Jin, Y. Yin, H. Zhang, C.Cai,Electrochimica Acta,2010, 55, 8606-8614.

[56] X. Wu, F. Zhao, J.R.Varcoe, A. E. Thumser, C. Avignone-Rossa, R.C. Slade, Bioelectrochemistry,2009, 77,64-68.